HOKKAIDO UNIVERSITY

Title	Interaction of electrons with light metal hydrides in the transmission electron microscope
Author(s)	Wang, Yongming; Wakasugi, Takenobu; Isobe, Shigehito et al.
Citation	Microscopy, 63(6), 437-447 https://doi.org/10.1093/jmicro/dfu034
Issue Date	2014-12
Doc URL	https://hdl.handle.net/2115/60028
Rights	This is a pre-copyedited, author-produced PDF of an article accepted for publication in [Microscopy] following peer review. The definitive publisher-authenticated version [Microscopy(Oxford) (2014)Vol.63,no.6, pp.437-447] is available online at: http://jmicro.oxfordjournals.org/content/63/6/437.long.
Type	journal article
File Information	Munuscript_W.pdf

Hokkaido University Collection of Scholarly and Academic Papers : HUSCAP

Interaction of electrons with light metal hydrides in the transmission electron microscope

Abstract

Transmission electron microscope (TEM) observation of light metal hydrides is complicated by the instability of these materials under electron irradiation. In this study, the electron kinetic energy dependences of the interactions of incident electrons with lithium, sodium, and magnesium hydrides, as well as the constituting element effect on the interactions, were theoretically discussed, and electron irradiation damage to these hydrides was examined using in-situ TEM. The results indicate that high incident electron kinetic energy helps alleviate the irradiation damage resulting from inelastic or elastic scattering of the incident electrons in the TEM. Therefore, observations and characterizations of these materials would benefit from increased, instead decreased, TEM operating voltage.

Keyword: transmission electron microscope, elastic scattering, inelastic scattering, light metal hydrides, electron irradiation

Introduction

The transmission electron microscope (TEM) is a very powerful observation and analysis tool for understanding the crystallographic, chemical and microstructural properties of materials, as well as directly measuring their characteristic sizes at the submicron- or nanoscale. Many processes can occur as the electron beam traverses the TEM specimen, including Bragg reflection, emissions of various electrons and X-rays, plasmon and phonon excitation, inter- and intraband transitions, ionization and radiolysis. The signals resulting from these phenomena allow for powerful microscopy and spectrometry applications in the TEM, e.g., imaging, diffraction, energy dispersive X-ray spectroscopy (EDS), and electron energy-loss spectrometry (EELS). However, these advantages are associated with detrimental beam damage, which limits the application of the TEM in materials that are sensitive to high-energy electron radiation.

Unfortunately, most advanced hydrogen storage materials consisting of light elements are partially subject to this limitation. To achieve a high hydrogen capacity [1-2], the majority of currently studied hydrogen storage materials are composed of compounds and complexes containing light elements [3] such as lithium, sodium, and magnesium. These materials are

generally unsuitable for TEM imaging because of the low contrast, arising from the smaller scattering factors of light elements, and their electron-beam sensitivity. However, TEM observation of hydrogen storage materials is vital for obtaining local information about phase transformations and microstructural changes during hydrogen absorption/desorption [4-9], which is very important for clarifying reaction mechanisms. Therefore, determining suitable conditions for the TEM observation of these materials is of practical significance.

Common practice for viewing beam-sensitive materials involves keeping the electron dose as low as reasonably practicable; therefore, the present work focuses on the relationship between TEM accelerating voltage and irradiation damage to hydrides. Although the use of low operating voltage is usually effective for observing materials composed of light elements, e.g., below 100 keV for carbon materials such as nanotubes [10-11] and graphene [12], this method may be unsuitable for observing light metal hydrides due to the excessively low threshold energy of displacement for hydrogen (and lithium), as well as the excessive energy transfer from incident electrons to hydrogen (and lithium) nuclei. In this study, the effects of constituting

element and incident-electron energy on the irradiation damage to lithium, sodium, and magnesium hydrides (LiH, NaH, and MgH_2) in the TEM were theoretically and experimentally investigated.

Theoretical discussion

Electron beam damage in the TEM is attributed to electron scattering in materials. When electrons bombard a material, the penetrating electrons interact with the constituent atoms by Coulomb forces, and some of these electrons are scattered as they change their direction of momentum and/or transfer energy to the material. The scattering caused by Coulomb interactions with atomic nuclei is referred to as elastic, whereas that due to Coulomb interactions with the atomic electrons surrounding each nucleus is said to be inelastic.

Microscopically, the damage initiated by elastic scattering of the incident electrons due to target nuclei consists mainly of atomic displacement, while the damage resulting from the inelastic scattering of incident electrons by atomic electrons is due to more complicated mechanisms such as the ionization of the target atom, atomic electron excitation, and plasmon and

phonon excitation. The macroscopic signs of beam damage appear as beam heating and radiolysis due to inelastic scattering, as well as structure ruin and surface sputtering due to elastic scattering. Microstructure change and decomposition (phase transformation and/or transition), as well as mass loss, are commonly observed.

The following theoretical discussion of relatively favorable conditions for the TEM observation of light metal hydrides therefore is from two broad categories: inelastic scattering damage and elastic scattering damage [13].

1. Inelastic scattering damage

Inelastic scattering damage in common TEM specimens usually presents as thermal destruction, i.e., a beam heating effect [14-16]. When incident electrons penetrate a material with the energy used for the TEM, their interactions with the atomic electrons in the material cause the excitation and ionization of the target atoms, converting most of the loss of incident energy into thermal energy [13]. This kind of energy transfer may decompose or even melt thermally sensitive specimens. In addition, the thermal effect also aggravates displacement damage.

Radiolysis, another type of irradiation damage triggered by the inelastic

scattering of electrons, may occur in hydrides and lead to their decomposition. Although radiolysis is particularly prevalent in biological and organic materials [17-18], the process can also damage inorganic specimens such as halides and oxides [19-20]. The occurrence of radiolysis in the hydrides of this study is difficult to be clarified due to its complicated mechanism. Nevertheless, the degree of damage due to either beam heating or radiolysis can be assessed by the loss of incident energy due to inelastic scattering, as quantified by electronic stopping power.

The stopping power for electrons traversing through matter represents the average rate of incident electron energy loss per unit of path length and includes two terms. The interaction of incident electrons with target atomic electrons can be calculated from Bethe's theory [21-22]; this term is called the 'collisional stopping power' and may be written as

$$S_{col} = \frac{2\pi e^4}{m_0 v^2} NZ[\ln \frac{m_0 v^2 E_0}{2I^2(1-\beta^2)} - (2\sqrt{1-\beta^2} - 1 + \beta^2)\ln 2 + 1 - \beta^2 + \frac{1}{8}(1-\sqrt{1-\beta^2})^2], \quad (1)$$

where E_0 is the kinetic energy of the incident electron, v the velocity of the incident electron, m_0 the electron rest mass, c the speed of light, e the elementary charge, $\beta = v/c$ is a relativistic term, and N, Z, and I are the number density, atomic number, and effective mean excitation energy of the

target atom, respectively. Additionally, the interaction between incident electrons and the target nucleus results in 'bremsstrahlung'; this stopping power is referred to as the 'radiative stopping power' and may be expressed as

$$S_{rad} = \frac{4NE_0Z(Z+1)e^4}{137{m_0}^2c^4}(\ln\frac{2{E_0}^2}{m_0c^2} - \frac{1}{3}) \text{ . (2)}$$

The sum of S_{col} and S_{rad} is called the 'total electronic stopping power'. The total electronic stopping powers of the hydrides versus incident electron energy were calculated using an NIST program [23] with a density-effect correction [24] and are shown in Fig. 1.

In Fig. 1, it may be clearly seen that the damage due to inelastic scattering in the low-energy region is more severe than that in the high-energy range and that the minimum damage to each hydride occurs at an incident electron energy of ~1 MeV. Therefore, high-voltage TEM operating at ~1 MeV should minimize the beam heating effect, whereas voltages in the conventional range would induce a severe effect.

2. Elastic scattering damage

For TEM specimens containing light elements, ballistic damage originating from knock-on displacement, which is subsequent to elastic scattering, is

consistently a major concern because the energy transfer from a high-angle elastic collision may easily exceed the energy needed to displace a light atom from its localized site. In general, the energy transfer in elastic scattering, i.e., the energy E lost by an incident electron and transferred to an atomic nucleus, may be expressed as

$$E = \frac{2E_0}{Mc^2}(E_0 + 2m_0c^2)\sin^2(\frac{\theta}{2}) = E_{\max}\sin^2(\frac{\theta}{2}) = E_{\max}(1-\cos\theta)/2, \quad (3)$$

where M is the mass of the target atom and θ is the scattering angle. E_{max} represents the maximum energy transfer, corresponding to a head-on collision (θ = 180°), and an exact relativistic extension gives the following equation [25]:

$$E_{\max} = \frac{E_0(E_0 + 2m_0c^2)}{E_0 + (1+m_0/M)^2 Mc^2/2} \approx \frac{2E_0}{Mc^2}(E_0 + 2m_0c^2). \quad (4)$$

Accordingly, E_{max} increases with increasing incident electron energy E_0 and decreasing nuclear mass M. The dependence of E_{max} on electron kinetic energy and atomic number are clearly shown in Fig. 2, as calculated using Eq. (4).

Ballistic damage in matter occurs when E_{max} exceeds the threshold displacement energy E_d, which is related to both atomic mass (or number) and atomic bonding energy. The threshold displacement energies and

melting points (MPs) of several materials are listed in Tab. 1.

As seen in Tab. 1, E_d largely falls within several dozen eV; the value decreases with MP due to weaker bonding energy and with atomic number due to lighter atomic weight. According to the MPs of Li, Na, Mg, as well as the decomposition temperatures of their hydrides (both listed in Tab. 2), it is reasonable to estimate that the E_d values of Li, Na, and Mg in their hydrides fall below 20 eV and that the E_d of the H atom in these hydrides is only several eV. As presented in Fig. 2, the E_{max} values of hydrogen and lithium are significantly larger than the threshold knock-on energy E_d values for these atoms, even at a low operating voltage of 100 keV, and are sufficient to cause displacement and hydrogen mass loss in all of the hydrides. Thus, the high E_{max} and low E_d values of the light elements, especially hydrogen, would result in hydride decomposition even at relatively low operating voltages in the TEM. Low TEM operating voltages, e.g., 60 keV for graphene [12], are conventionally effective for reducing knock-on damage, but the E_{max} of hydrogen and lithium cannot be reduced below their E_d values in an usual TEM. Lowering the operating voltage to avoid ballistic damage to hydrides is therefore ineffective and would encounter problems with electron elastic

scattering cross-section, which governs the probability of the elastic scattering event and also impacts ballistic damage.

The intensity of the atomic elastic scattering of electrons is inversely proportional to the electron kinetic energy and diminishes with the atomic mass of the target atom [30]. The cross-section of the elastic scattering is impacted by the same factors. The total electron elastic scattering cross-sections of the light elements for various electron kinetic energies were calculated and are listed in Tab. 3 [31]. The maximum value was calculated for Mg at 100 keV and the minimum for H at 300 keV. In fact, high accelerating voltages reduce the total cross-sections of the light elements. However, the cross-section of atomic displacement is not monotonically dependent on accelerating voltage and atomic mass.

The cross-section of primary knock-on atom (PKA) formation can be calculated by the following equation [32]

$$\sigma_p = 4\pi(\frac{Za_0E_R}{m_0c^2})^2 \frac{1-\beta^2}{\beta^4}[(\frac{E_{\max}}{E_d}-1)-\beta^2\ln(\frac{E_{\max}}{E_d})+\pi\alpha\beta\{2[(\frac{E_{\max}}{E_d})^{1/2}-1]-\ln(\frac{E_{\max}}{E_d})\}], \quad (5)$$

where a_0 is the Bohr radius, E_R is the Rydberg energy, and $\alpha = Z/137$. Fig. 3 shows the electron energy dependence of the PKA formation cross-sections of the light elements using an E_d value of 10 eV. The cross-sections of Mg and

Na rapidly rise as electron energy increasing from ~100 keV but flatten out gradually after 200 keV, with no significant difference between 200 keV and 1,000 keV. In contrast, Li and H, which is contained in every hydride, displayed radically different relationships between cross-section and electron energy: the PKA formation cross-sections of these elements monotonically decrease with increasing electron energy in the available TEM range. The results indicate that high accelerating voltage can reduce the displacement of H and Li and do not make the issue more serious for Na and Mg atoms.

For specimens consisting of light elements, surface sputtering is another type of ballistic damage that occurs on the specimen surface. This phenomenon occurs easily and leads to the majority of mass loss in these specimens because the energy transfer needed to sputter a surface atom is less than that required for the displacement of a bulk atom. Sputter rate (thickness of mass loss per second), which has been discussed and calculated for carbon in the literature [13], follows a similar pattern to that of the PKA formation cross-section in kinetic energy dependence, i.e., a high sputter rate occurs at the low electron energy range of 100 - 200 keV. This result suggests that rapid hole drilling could occur in LiH specimens in conventional TEM

due to the high E_{max} and low E_d values of H and Li.

Experimental investigation

Experimental

The samples investigated for electron beam damage in this study consisted of LiH (purchased from Sigma-Aldrich, 94% purity), NaH (purchased from Sigma-Aldrich, 95% purity), and MgH_2 (purchased from Alfa Aesar, 98% purity) in powder form. All of the samples were handled in a high-purity, argon-filled glove box to minimize oxidation and water adsorption.

In the glove box, each TEM specimen was prepared by sprinkling dry powder on a copper grid and then mounting the grid in a TEM holder. The holder was subsequently transferred from the glove box into the TEM in a sealed, Ar-filled plastic bag to avoid oxidation and hydroxylation, as described in detail elsewhere [33]. The investigation of electron beam damage to the samples was performed using a conventional TEM (JEOL, JEM-2010), operated at an accelerating voltage of 200 keV for LiH, NaH, and MgH_2 to clarify the constituting element effect and at 100 keV for NaH to determine the electron energy effect on irradiation damage to the hydrides.

In addition, fine grains of NaH, obtained by the in-situ thermal decomposition of sodium alanate [34], were observed using a high-voltage TEM (HVEM, JEOL JEM-ARM1300) to investigate the stability of NaH and the possibility of obtaining a high-resolution image of this hydride at the high accelerating voltage of 1250 keV.

This study focused on investigating the electron beam damage to the hydrides and the role of accelerating voltage; no deliberate attempt was made to reduce the electron dose, and a normal total dose of 75 C/cm^2 was selected as the irradiation condition. This dose is nearly equivalent to that obtained during the routine operation of the TEM at a magnification of x150,000 with normal brightness for one operation from centering the sample to acquiring the image; x150,000 is a commonly used magnification for observing nanomaterials and nanostructures. To match the sample sizes, the electron irradiation at both 100 and 200 keV was practically implemented at the indicated magnification of x50,000 for 2 minutes at a current density of 0.625 A/cm^2 (i.e., a total dose of 75 C/cm^2), forming an irradiation beam of ~1.5 μm in diameter with a nearly uniform intensity distribution. This beam profile is shown in Fig. 4.

Results and discussion

Fig. 5 shows the results of irradiating LiH, NaH, and MgH_2 with a 200 keV accelerated electron beam at an electron dose of 75 C/cm^2. Among the three hydrides, LiH presented the most typical ballistic damage, with the most violent shape change and greatest volume reduction due to mass loss, as shown in Fig. 5 (a) and (b). The much greater maximum energy transfer E_{max} (Fig. 2) and low threshold displacement energy E_d values of hydrogen and lithium were presumably accountable for the severe knock-on damage to LiH. The electron diffraction from the irradiated LiH sample confirmed the existence of lithium metal, indicating that the hydride was decomposed forcibly by electron irradiation, and the relatively slower mass loss rate of lithium metal compared with that of hydrogen caused it to remain in the sample. Similarly, the NaH sample under the same irradiation conditions also experienced volume shrinkage accompanied by the decomposition of NaH to sodium metal, as shown in Fig. 5 (c) and (d). However, NaH showed greater beam heating. The growth of a platelike product was observed during irradiation. This irradiation product, as shown in Fig. 5(d), was verified as sodium through its electron diffraction pattern. As will be discussed in this

section, the formation of this area likely resulted from the melting of sodium metal that remained after hydride decomposition due to knock-on damage. Comparatively, MgH_2 showed the greatest resistance to electron beam damage among the hydrides. As shown in Fig. 5 (e) and (f), no obvious changes in volume and shape were observed for this hydride after irradiation at 200 keV under the same conditions. However, MgH_2 was undoubtedly decomposed by electron irradiation. Transformation from the MgH_2 phase to the Mg metal phase was verified by electron diffraction pattern, as presented in the insets of Fig. 5 (e) and (f): MgH_2 had a twin structure that retrogressed into the poly-crystal structure of Mg metal. As indicated above, the inevitable displacement of hydrogen by the incident electrons led to the decomposition of the hydrides into elemental metals, which subsequently presented varied behaviors under irradiation due to their different properties. The lightest metal, lithium, was easily knocked-on and sputtered by incident electrons and rapidly lost its remaining volume, whereas the heaviest metal, magnesium, almost completely resisted the irradiation and retained its appearance despite its nearly maximum PKA cross-section at 200 keV. Although the hydride stopping power, maximum energy transfer

E_{max}, and PKA formation cross-section of sodium were almost the same as those of magnesium, as previously discussed in the theoretical section, only sodium presented the typical result of beam heating (i.e., melting) due to its low MP.

The energy transfer from the inelastic scattering of the incident electrons may have resulted in the melting of the sodium metal derived from the decomposed NaH. The serial diffraction patterns in Fig. 6 obtained by converging the beam to ~400 nm in diameter at 200 keV clearly revealed the process of irradiation damage to the NaH sample from the decomposition of NaH through the melting of sodium. Although decomposition also occurred in the LiH and MgH_2 samples, liquefied Li and Mg metals were not found during electron irradiation in this study. Thus, the beam heating effect is limited to the temperature range of 98 - 180 ºC, as estimated by the MPs of the elementary metals listed in Tab. 2. However, the decomposition temperatures of these hydrides easily exceed the range of the beam heating effect, indicating that decomposition did not result from beam heating. Therefore, the main mechanism of hydride decomposition is the ballistic damage due to the elastic scattering of the incident electrons. The irradiation

damage of the NaH sample due to a focused beam could lead to hole drilling through a different mechanism, the melting of sodium.

Fig. 7 shows the hole drilling TEM micrographs of NaH (a) and LiH (b) samples at an operating voltage of 200 keV. Hole drilling was, however, absent in the MgH_2 sample. The holes formed rapidly, within several seconds for both the NaH and LiH samples, but a hole with a distinct outline was drilled in the LiH sample, while the hole drilled in the NaH sample was shaded by thin films of sodium. This difference resulted from the different hole-drilling mechanisms. The rapid hole drilling observed in the NaH sample was due to the melting of sodium following NaH decomposition by ballistic damage, as mentioned above, while the process in the LiH specimen was dominated by surface sputtering, because lithium is much more easily sputtered by an electron beam due to its low E_d and high $E_{max,}$ as shown in Fig. 2. Electrostatic charging has been proposed as the mechanism for hole drilling in some insulators [35], but surface sputtering due to atomic displacement was responsible for the hole drilling in the present work. Hole drilling did not occur in the MgH_2 specimen, while in the NaH specimen, it resulted from the melting of sodium after the removal of hydrogen atoms via

knock-on processes. These results indicated that hole drilling in hydrides should be due to surface sputtering and not radiolysis, as the process is dependent on atomic number and not conductivity.

Besides the knock-on damage and the beam heating effect previously described, it is beyond the scope of this study, but also worth noting that magnesium oxide was formed accompanying with the decomposition of MgH_2 by irradiation, as clearly shown in the diffraction pattern inset in Fig. 5(f). This oxide formation should be attributed to neither elastic nor inelastic scattering damage but instead to chemical damage, the mechanism of which has been well described in the literature [11]. Similar phenomena also occurred in the LiH and NaH specimens, e.g., the Debye-Scherrer rings of Li_2O clearly appeared in the diffraction pattern shown in Fig. 5(b).

On the basis of the observation results of irradiation damage to the hydrides at 200 keV, NaH was determined as appropriate for investigating the effect of incident electron energy on irradiation damage because it is noticeably sensitive to both knock-on damage and beam heating. Fig. 8 shows the damage to NaH under irradiation at an accelerating voltage of 100 keV. A comparison of (a) and (b) in Fig. 8 indicates that the volume of NaH

was greatly reduced after irradiation at 100 keV as compared with 200 keV. The majority of the volume shrinkage was due to beam heating, a typical form of inelastic scattering damage, because the cross-section of PKA formation for sodium is close to zero at 100 keV (see Fig. 3); the intense beam heating effect at this voltage coincides with the prediction of Fig. 1. Indeed, the visible melting of Na, which appeared as a fluidlike flow in the irradiated area, was often observed during the irradiation. Fig. 8(c) shows a large platelike particle formed in the edge zone of the irradiated area after irradiation, which was determined to be a single crystal of sodium by the inset of the diffraction pattern. These results were different from those observed under irradiation at 200 keV: elemental sodium particles were often formed away from the irradiation center because of the stronger beam heating effect at 100 keV.

For HVEM observation, the fine-grained NaH obtained by the in-situ thermal decomposition of sodium alanate was chosen as the sample, because the particle size of the originally purchased NaH was too big (and hence too thick) for high-resolution observation. In contrast with the decomposition of NaH and the melting of Na, as well as the hole drilling observed at the low

kinetic energy range in the TEM, the fine-grained NaH exhibited surprisingly strong resistance to the electron beam at the operating voltage of 1250 keV. Indeed, in a previous study [34], NaH was often found instead of sodium using HVEM observation after the in-situ thermal decomposition of sodium alanate. Fig. 9 shows a high-resolution image of the fine-grained NaH specimen obtained by the HVEM at 1250 keV. As high-resolution images are always obtained at high magnifications under high current density irradiation, the success of the high-resolution imaging proves the stability of NaH at 1250 keV even under a harsher current density condition (~1.6 A/cm^2). This result was likely due to the low values of the stopping power of NaH and the cross-section of hydrogen PKA formation at the high voltage of 1250 keV, as well as the size of the fine particles. As indicated in Fig. 2, although the E_{max} values of hydrogen and lithium are certainly larger at high voltage, these values also greatly exceed the threshold values of displacement for these elements in the low voltage range and are sufficiently high to severely damage the sample once the PKA forms frequently. Therefore, for irradiation with the same electron dose, lowering TEM operating voltage is ineffective for decreasing the ballistic damage to

hydrides; the only way to mitigate the damage is to reduce the probability of PKA formation, namely, to reduce the PKA formation cross-section and sample thickness. A small cross-section of PKA formation is synonymous with a long mean free path of PKA formation for incident electrons, while a thin sample indicates a short absolute path. Thus, only thin samples of the hydrides may be observed using the TEM with little displacement of hydrogen and/or lithium regardless of accelerating voltage, while the HVEM is more advantageous for observation. Moreover, the suppression of the beam heating effect at high voltage should also be helpful for decreasing displacement damage, the degree of which is usually dependent on temperature.

Concluding remarks

In this study, the inelastic scattering damage to light metal hydrides in the TEM was theoretically assessed according to electronic stopping power, while the elastic scattering damage was determined based on the maximum energy transfer and PKA formation cross-section of the light atoms in the hydrides. The actual damage to these hydrides was then investigated

experimentally. The results indicate that lowering the operating voltage is ineffective for avoiding the decomposition of hydrides due to the displacement of hydrogen, while high incident electron kinetic energy alleviates the irradiation damage due to inelastic and elastic scattering but requires thin (or fine-particle) samples. The high resolution imaging at 1250 keV shown in Fig. 9 indicates that a high operating voltage of around 1000 keV, in light of the minimum electronic stopping power of the hydrides and small hydrogen cross-section of PKA formation, is more suitable for observing hydrides. In fact, for thermally sensitive hydrides, a higher voltage can also decrease the irradiation damage even at a relatively low energy range, as shown by the results for NaH at 100 and 200 keV.

It should be noted that no completely nondestructive technique exists for observing hydrides (or similar materials). The damage caused during observation can be mitigated by reducing the electron dose through a beam of lower current density or a shorter irradiation time, as well as by using a favorable accelerating voltage. In addition, coating the specimen with conducting materials such as carbon could reduce surface sputter and the damage related to electrostatic charging, while using a cold finger would

effectively reduce the chemical damage to specimens sensitive to the background gases in the TEM [11].

Acknowledgements

A part of this work was conducted at Hokkaido University, partially supported by 'Nanotechnology Platform' Program of the Ministry of Education, Culture, Sports, Science and Technology (MEXT), Japan.

References

1 http://www1.eere.energy.gov/hydrogenandfuelcells/storage/index.html

2 http://www.nedo.go.jp/activities/FF_00518.html

3 Yang J, Sudik A, Wolverton C, and Siecel D J (2010) High capacity hydrogen storage materials: attributes for automotive applications and techniques for materials discovery. *Chem.Soc. Rev.* **39**, 656-675.

4 Banerjee A N, Joo S W, and Min B K (2013) Ambient-temperature fabrication of microporous carbon terminated with graphene walls by sputtering process for hydrogen storage applications. *Thin Solid Films* **537**, 49–57.

5 Danaie M and Mitlin D (2009) TEM analysis and sorption properties of high-energy milled MgH2 powders. *J. Alloy. Compd.* **476**, 590–598.

6 Danaie M, Tao S X, Kalisvaart P, and Mitlin D (2010) Analysis of deformation twins and the partially dehydrogenated microstructure in nanocrystalline magnesium hydride (MgH2) powder. *Acta Mater.* **58**, 3162–3172.

7 Jeon K J, Moon H R, Ruminski A M, Jiang B, Kisielowski C, Bardhan R, and Urban J J (2011) Air-stable magnesium nanocomposites provide rapid and high-capacity hydrogen storage without using heavy-metal catalysts. *Nat. Mater.* **10**, 286–290.

8 Porcu M, Petford-Long A K, and Sykes J M (2008) TEM studies of Nb2O5 catalyst in ball-milled MgH2 for hydrogen storage. *J. Alloy. Comp.* **453**, 341–346.

9 Wakasugi T, Isobe S, Umeda A, Wang Y, Hashimoto N, and Ohnuki S (2013) Development and application of a window-type environmental cell in high voltage electron microscope. *J. Alloy. Compd.* **580**, S127-S130.

10 Smith B and Luzzi D (2001) Electron irradiation effects in single wall carbon nanotubes. *J. Appl. Phys.* **90**, 3509-3515.

11 Mølhave K, Gudnason S, Pedersen A, Clausen C, Horsewell A and Bøggild P (2007) Electron irradiation-induced destruction of carbon nanotubes in electron microscopes. Ultramicroscopy 108, 52-57.

12 Wang H, Li K, Yao Y, Wang Q, Cheng Y, Schwingenschlögl U, Zhang X and Yang W (2012) Unraveling the atomic structure of ultrafine iron clusters. Sci. Rep. 2, 995.

13 Egerton R F, Li P, and Malac M (2004) Radiation damage in the TEM and SEM. *Micron* **35**, 399–409.

14 Talmon Y and Thomas E L (1977) Beam heating of a moderately thick cold stage specimen in the SEM/STEM. *J. Microsc.* **111**, 151–164.

15 Pantano C G and Madey T E (1981) Electron beam damage in Auger electron spectroscopy. *Applications of Surface Science* **7**, 115–141.

16 Liu M, Xu L, and Lin X (1994) Heating effect of electron beam bombardment. *Scanning* **16**, 1–5.

17 Cosslett, V E (1978) Radiation damage in the high resolution electron microscopy of biological materials: A review*. *J. Microsc.* **113**, 113–129.

18 Glaeser R M and Taylor K A (1978) Radiation damage relative to transmission electron microscopy of biological specimens at low temperature: a review. *J. Microsc.* **112**, 127–138.

19 Egerton R F, Crozier P A, and Rice P (1987) Electron energy-loss spectroscopy and chemical change. *Ultramicroscopy* **23**, 305–312.

20 Hobbs L W (1979) Application of transmission electron microscopy to radiation damage in ceramics. *J. Am. Ceram. Soc.* **62**, 267–278.

21 Bethe H (1930) Theory of the passage of fast corpuscular rays through matter (in German). *Annalen der Physik* **5**, 325–400.

22 Bethe H (1933) *Handbook of Physics* Vol. **24** (Springer, Berlin)

23 National Institute of Standards and Technology (NIST), *ESTAR* Program: http://physics.nist.gov/PhysRefData/Star/Text/ESTAR.html

24 Sternheimer R, Seltzer S, and Berger M (1982) Density effect for the ionization loss of charged particles in various substances. *Phys. Rev. B* **26**, 6067–6076.

25 Banhart F (1999) Irradiation effects in carbon nanostructures. *Rep. Prog. Phys.* **62**, 1181–1221.

26 Hobbs LW (1987) Radiation effects in analysis by TEM. In: *Introduction to Analytical Electron Microscopy*, ed. Hren J J, Goldstein, J I, and Joy D C, pp399-445, (Plenum Press, New York).

27 Johnson D (2002) *Metals and Chemical Change* Vol. **1** (Royal Society of Chemistry, London).

28 Šubert J and Tobola K (1976) DTA study of the kinetics of sodium hydride decomposition. *J. Therm. Anal.* **10**, 5-12.

29 Sakintuna B, Lamari-Darkrim F, Hirscher M (2007) Metal hydride materials for solid hydrogen storage: A review. *Int. J. Hydrogen Energy* **32**, 1121-1140.

30 Hirsch P B, Howie A, Nicholson R B, Pashley D W, and Whelan M J (1965) *Electron Microscopy of Thin Crystals*. (William Clowes & Sons Ltd, London and Beccles).

31 National Institute of Standards and Technology (NIST) Standard Reference Database 64: *Electron Elastic-Scattering Cross-Section Database* (version 3.1).

32 McKinley W and Feshbach H (1948) The Coulomb Scattering of Relativistic Electrons by Nuclei. *Phys. Rev.* **74**, 1759–1763.

33 Yao H, Isobe S, Wang Y, Hashimoto N, and Ohnuki S (2011) Plastic bag method for active sample loading into transmission electron microscope. *J. Electron Microsc.* **60**, 375–378.

34 Yao H, Kawasaki H, Isobe S, Wang Y, Hashimoto N, and Ohnuki S (2010)

High-resolution TEM observations of the decomposition of NaAlH4. *Mater. Trans.* **51**, 1016–1019.

35 Humphreys C J (1990) Electron beam nano-etching in oxides, fluorides, metals and semiconductors. *Scanning Microscopy Supplement* **4**, 185-192.

36 International Crystal Structure Database (ICSD): 02-0809.

Tables

Table 1. Threshold displacement energies (E_d) [26] and MPs of several materials

Elements	Al	Fe	Cu	Mo	W	Pb	Graphene
E_d (eV)	25	40	30	60	90	25	17 [12]
MP (°C)	660	1536	1084	2617	3467	327	----

Table 2. MPs of the elementary metals and decomposition temperatures of their hydrides

Elementary metal	MP (°C)	Hydride	Decomposition temperature (°C)
Li	180.55	LiH	> 900 [27]
Na	97.85	NaH	500–800 [28]
Mg	648.85	MgH_2	300–400 [29]

Table 3. Total electron elastic scattering cross-sections of the light elements (10^{-20} cm^2) for different accelerating voltages

Elements	100 (keV)	200 (keV)	300 (keV)
H	3.61	2.25	1.80
Li	35.80	22.24	17.83
Na	154.93	96.57	77.56
Mg	201.92	125.92	101.12

Figure legends

Figure 1
The total electronic stopping powers of LiH, NaH, and MgH_2 versus incident electron energy. The stopping powers of NaH and MgH_2 are significantly higher than that of LiH, but the minimum value is ~1 MeV for all hydrides.

Figure 2
The maximum energy transfer (E_{max}) versus atomic number at different electron accelerating voltages. The E_{max} values of hydrogen and lithium are very high and significantly exceed the threshold values of displacement, even at 100 kV.

Figure 3
The dependences of the PKA formation cross-sections of H, Li, Na, and Mg atoms on incident electron energy. The cross-sections of PKA formation for hydrogen and lithium differ from those of the other atoms, decreasing as the energy of incident electrons increases over the practical operating voltage range of the TEM.

Figure 4
The beam profile of the irradiation beam along the dotted line at the indicated magnification of x50,000 with a current density of 0.625 A/cm^2 under an operating voltage of 200 keV. The beam is ~1.5 μm in diameter with an almost uniform intensity distribution.

Figure 5
TEM images of LiH, NaH, and MgH_2 (from top to bottom) obtained at 200 keV before (left side) and after (right side) electron irradiation for 2 minutes. The insets represent electron diffraction patterns. The diffraction spots in the insets of (a), (c), and (e) confirmed that the samples were LiH, NaH, and MgH_2, respectively. The pattern in (e) shows a twin structure in the MgH_2 sample. The spots in the insets of (b), (d), and (f) confirmed the formation of elemental Li, Na, and Mg, respectively, after irradiation. The single-crystal pattern from the circled area in (d) confirmed that the platelike phase was

sodium. In addition, the Debye-Scherrer rings in the diffraction patterns of (b) and (f) correspond to Li_2O and MgO, respectively.

Figure 6
The serial diffraction patterns of the NaH sample obtained by converging the beam to ~400 nm in diameter at 200 keV. The diffraction spots corresponding to the crystal phase in pattern (a) rapidly faded (b) to become a broad, hollow ring pattern (c) corresponding to the liquid phase.

Figure 7
TEM images of (a) NaH and (b) LiH samples after hole drilling by a focused beam operated at 200 keV. The hole in LiH has a distinct outline, while the hole in NaH is shaded by thin films formed from melted sodium.

Figure 8
TEM images of NaH obtained at 100 keV before (a) and after (b) electron irradiation. The volume of NaH in (a) was significantly reduced, as shown in (b), by the irradiation. An example of sodium melting is shown in (c). A large platelike particle formed away from the irradiation center after irradiation, and the inset diffraction pattern confirmed that the particle was a single crystal of sodium.

Figure 9
High-resolution image obtained from a sample of in-situ thermally decomposed sodium alanate (a) and the selected area diffraction pattern (SADP) from the irradiated area (b). The operating voltage was 1250 keV. The lattice fringes in (a) correspond well with the (111) and (220) crystal planes of sodium hydride [36], the presence of which was confirmed by the SADP (b). Note that the aluminum identified in the SADP is produced along with NaH by the thermal decomposition of sodium alanate.

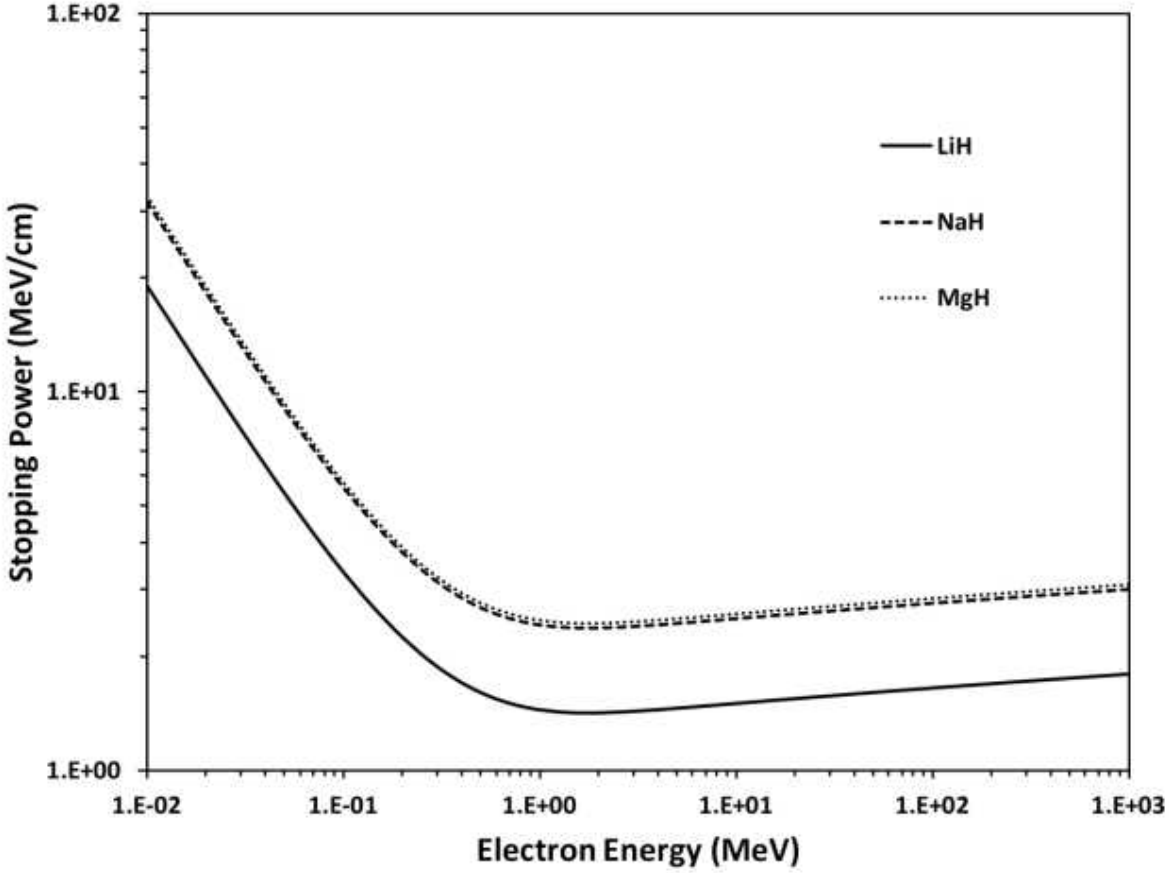

1.E+02
1.E+01
1.E+00
Stopping Power (MeV/cm)
LiH
NaH
MgH
1.E-02
1.E-01
1.E+00
1.E+01
1.E+02
1.E+03
Electron Energy (MeV)

Fig. 1

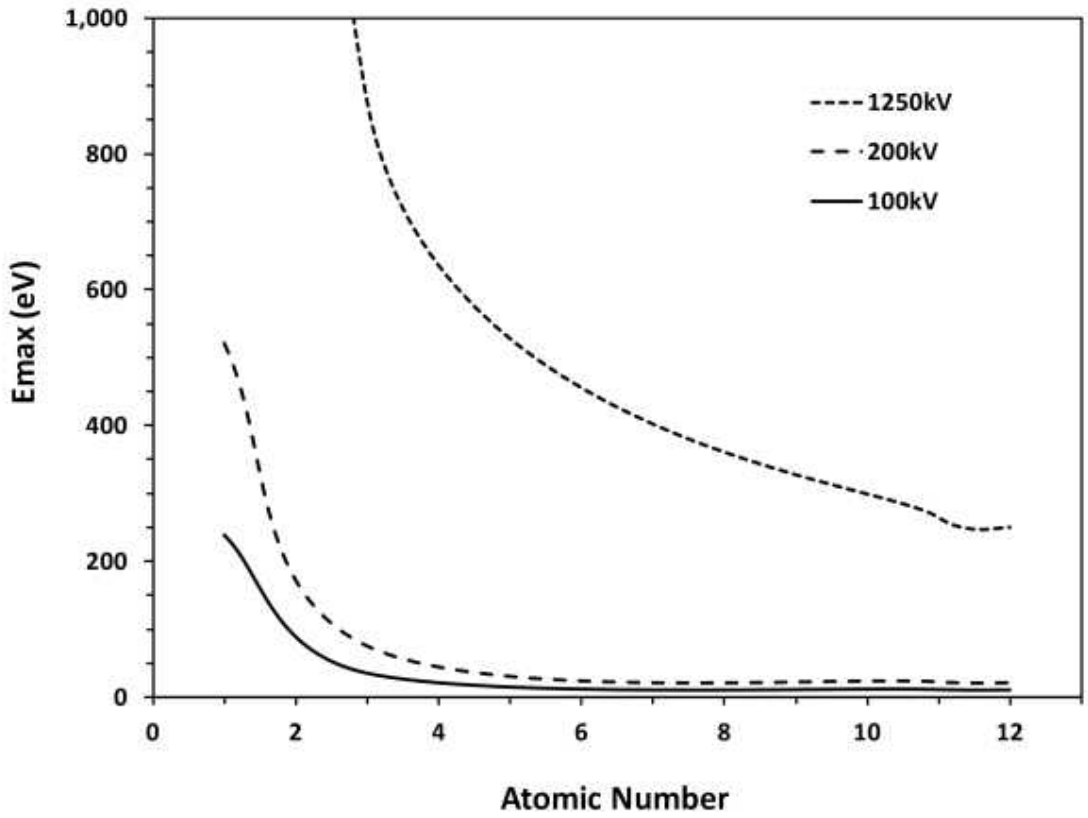

1,000
800
600
400
200
0
Emax (eV)
0
2
4
6
8
10
12
Atomic Number
1250kV
200kV
100kV

Fig. 2

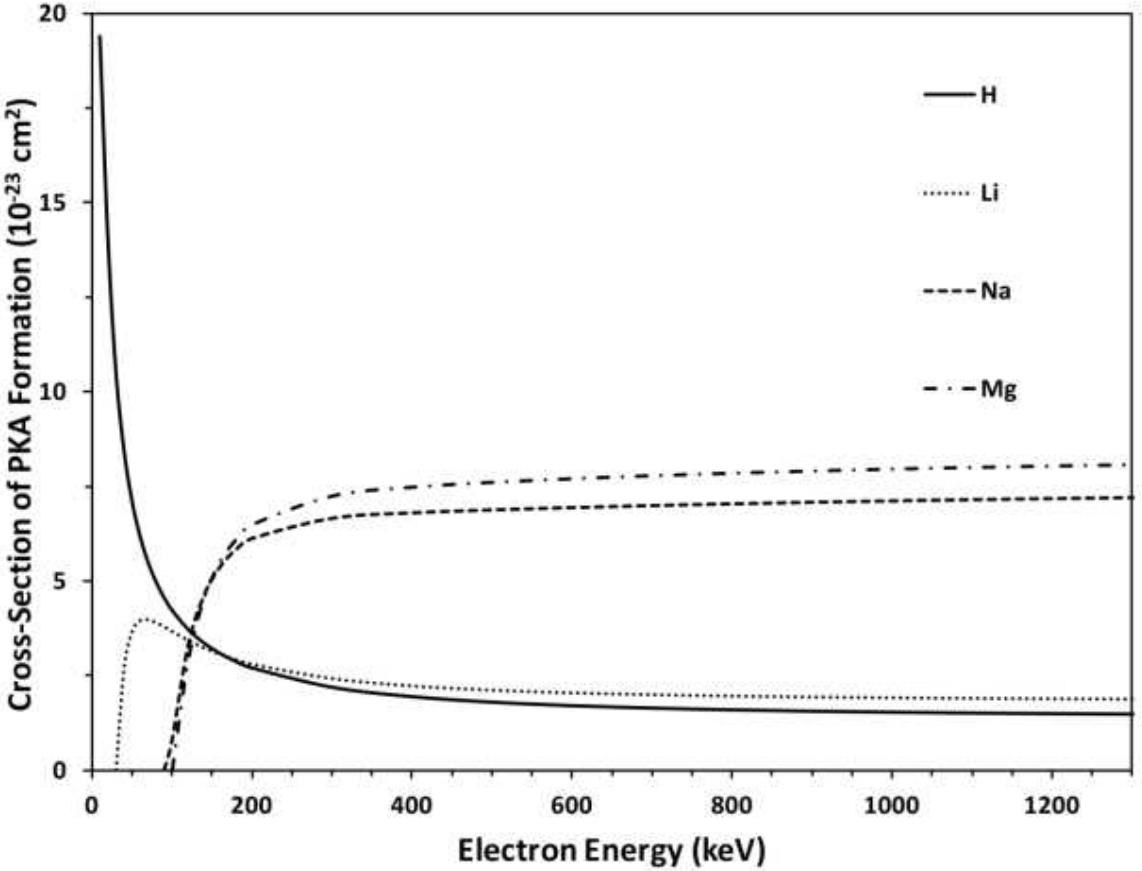

Cross-Section of PKA Formation (10^{-23} cm^2)
Electron Energy (keV)
H
Li
Na
Mg
0
5
10
15
20
0
200
400
600
800
1000
1200

Fig. 3

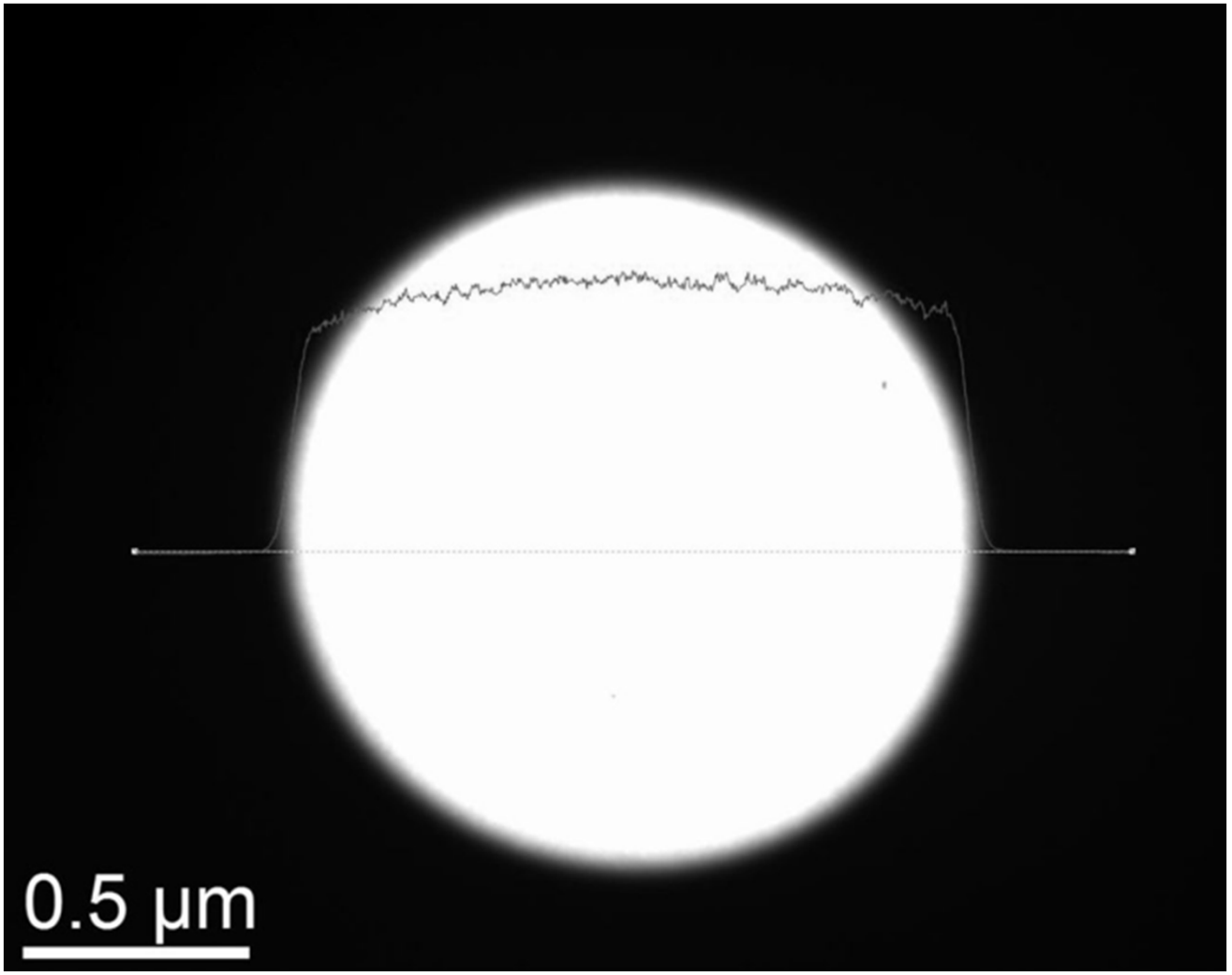


Fig. 4

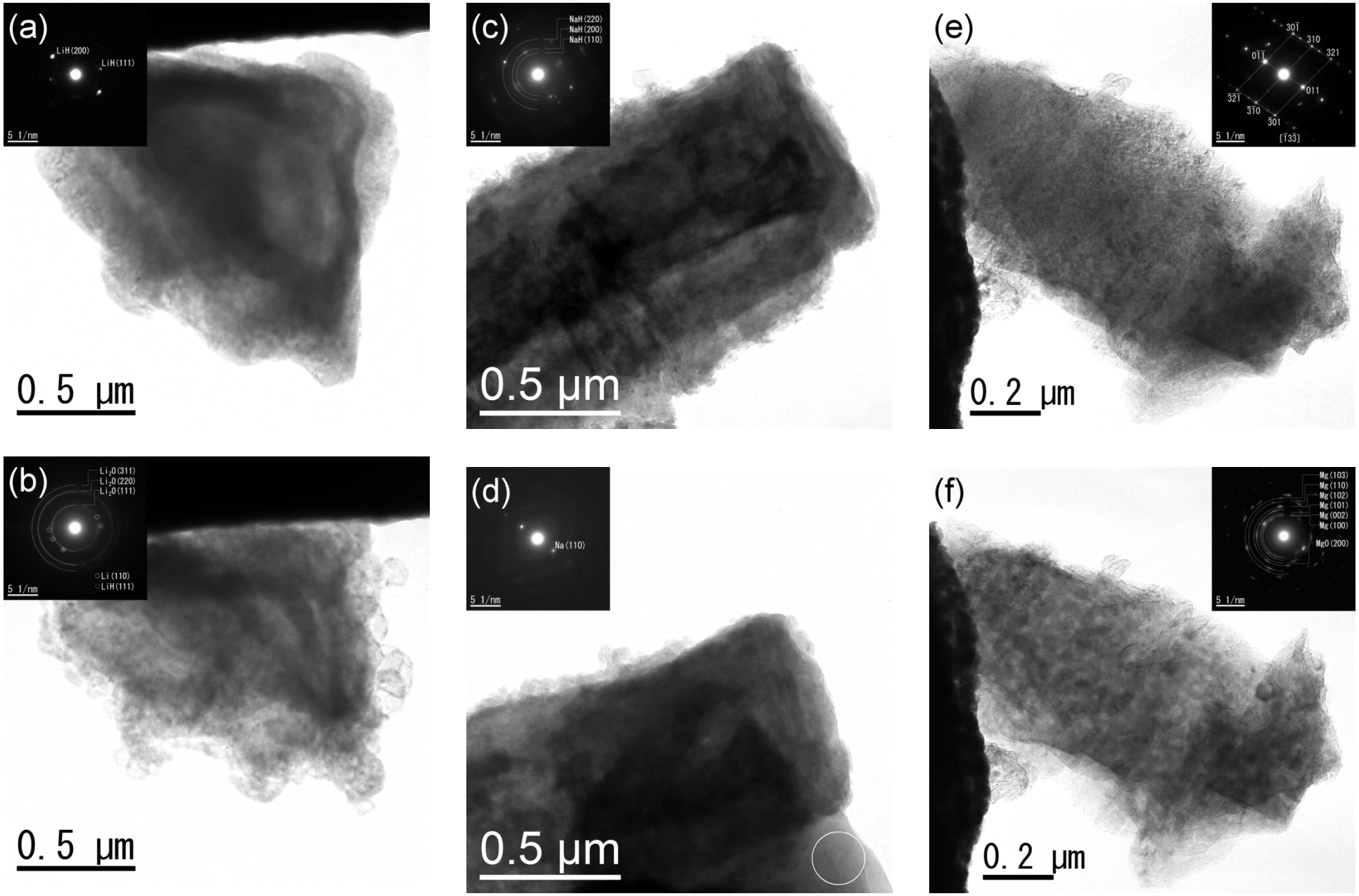

(a)
LiH(200)
LiH(111)
5 1/nm
0.5 μm
(c)
NaH(220)
NaH(200)
NaH(110)
5 1/nm
0.5 μm
(e)
5 1/nm
0.2 μm
(b)
Li2O(311)
Li2O(220)
Li2O(111)
Li(110)
LiH(111)
5 1/nm
0.5 μm
(d)
Na(110)
5 1/nm
0.5 μm
(f)
Mg(103)
Mg(110)
Mg(102)
Mg(101)
Mg(002)
Mg(100)
MgO(200)
5 1/nm
0.2 μm

Fig. 5

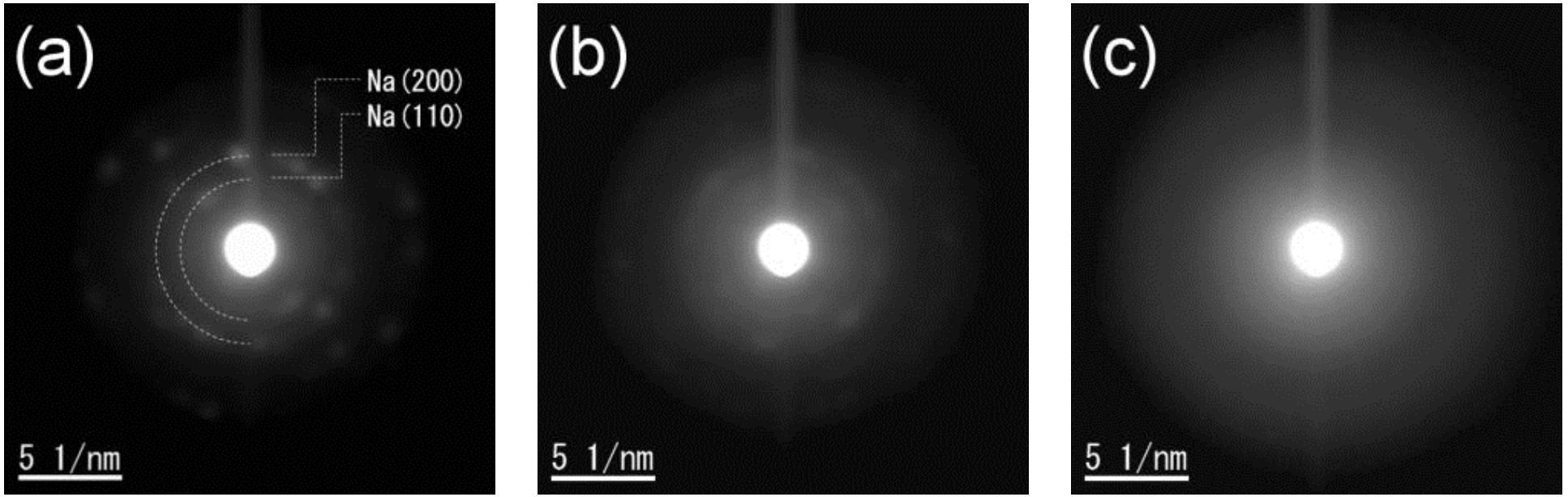


Fig. 6

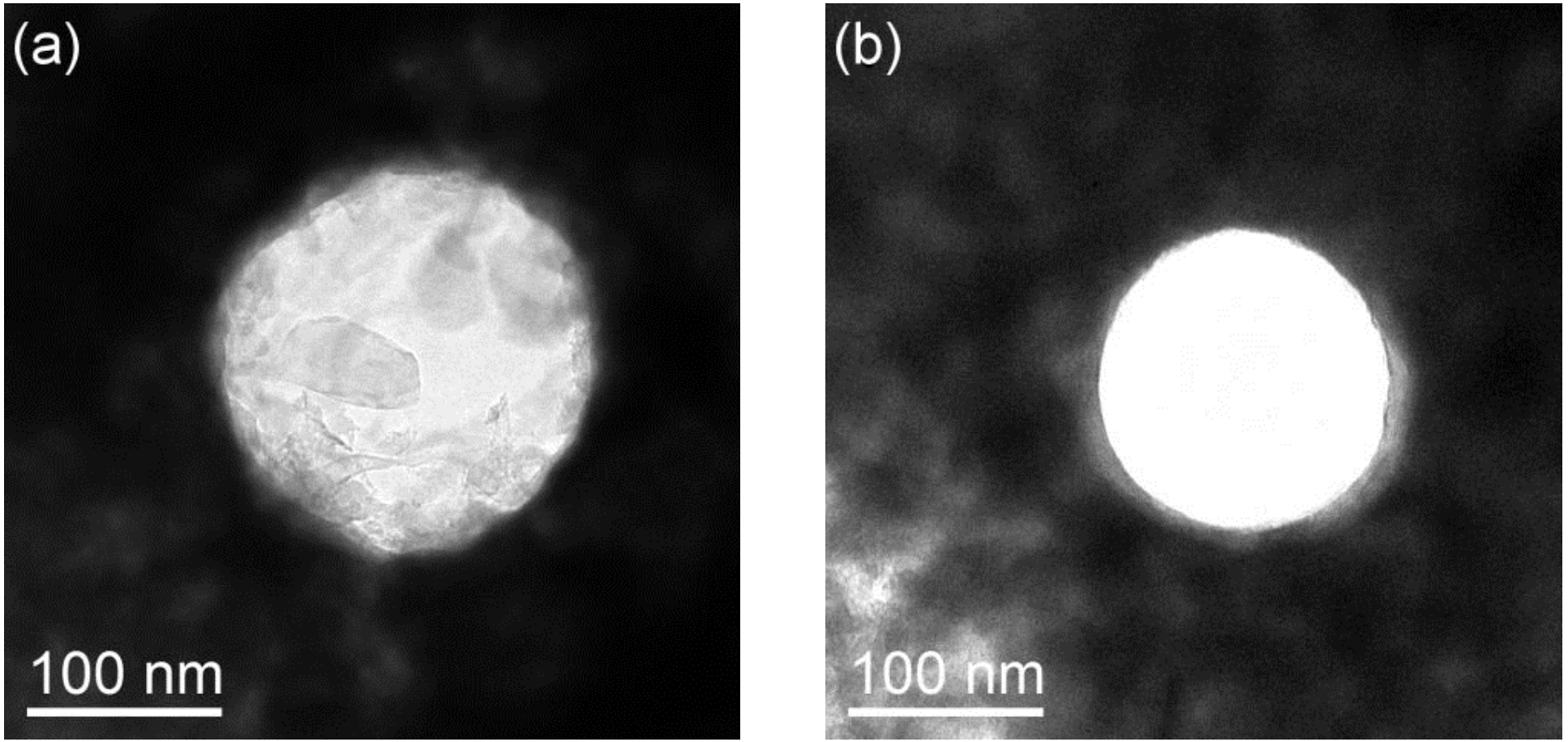


Fig. 7

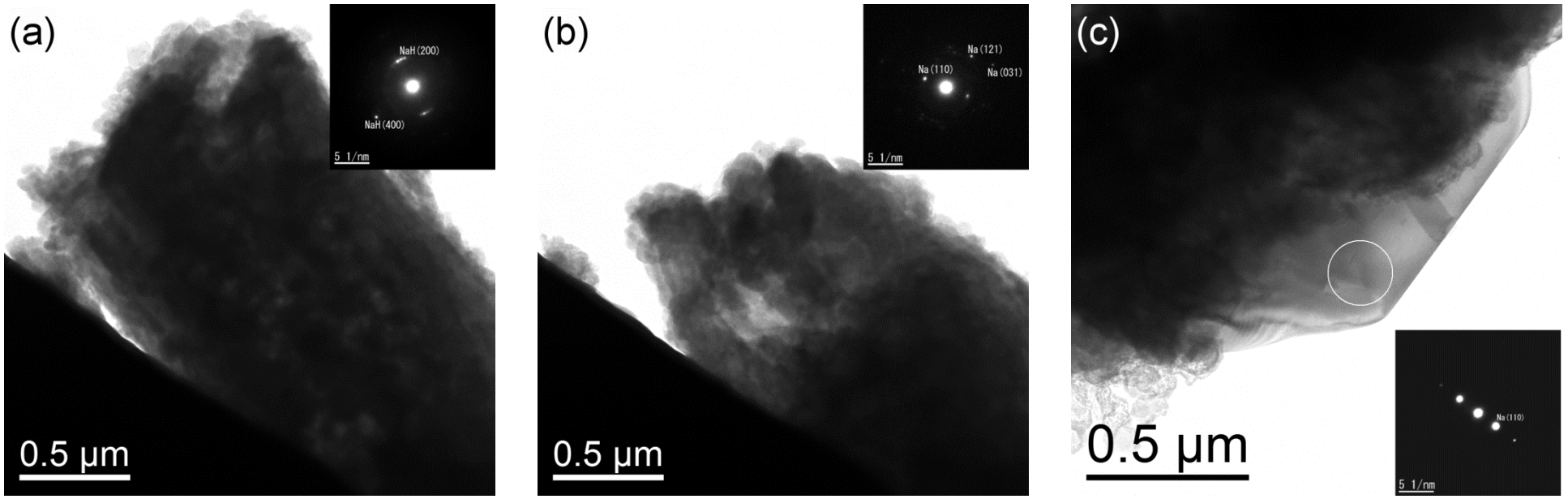

(a)
NaH (200)
NaH (400)
5 1/nm
0.5 μm
(b)
Na (121)
Na (110)
Na (031)
5 1/nm
0.5 μm
(c)
0.5 μm
Na (110)
5 1/nm

Fig. 8

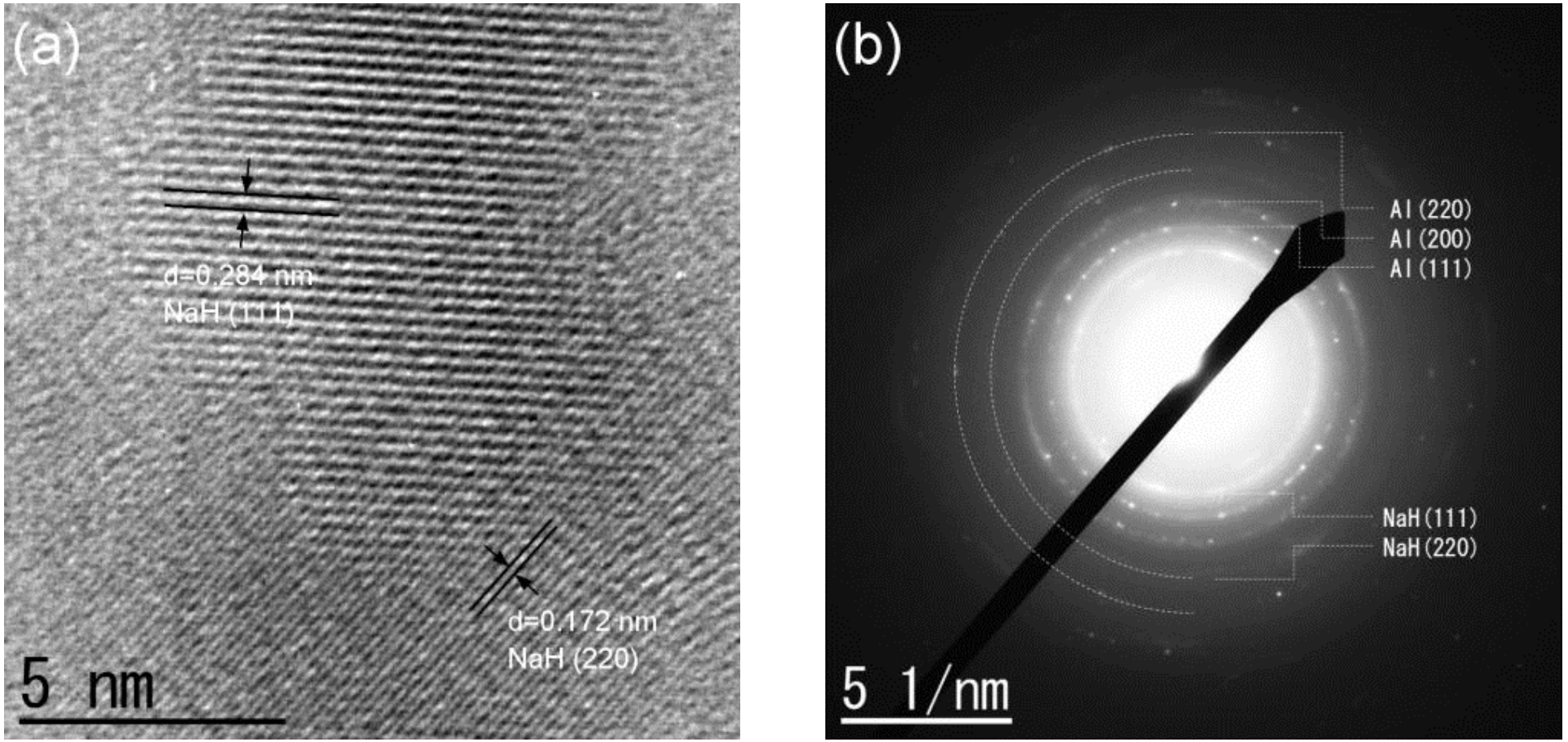

(a)
d=0.284 nm
NaH (111)
d=0.172 nm
NaH (220)
5 nm
(b)
Al (220)
Al (200)
Al (111)
NaH (111)
NaH (220)
5 1/nm

Fig. 9